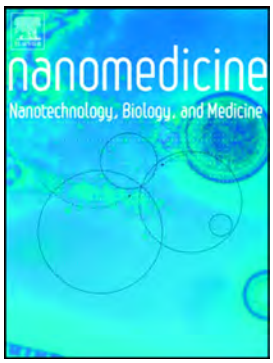

Unambiguous detection of atherosclerosis using bioorthogonal nanomaterials

Juan Pellico, Irene Fernández-Barahona, Marina Benito, Ángel Gaitán-Simón, Lucía Gutiérrez, Jesús Ruiz-Cabello, Fernando Herranz

PII: S1549-9634(19)30008-5
DOI: https://doi.org/10.1016/j.nano.2018.12.015
Reference: NANO 1929

To appear in: *Nanomedicine: Nanotechnology, Biology, and Medicine*

Revised date: 13 December 2018

Please cite this article as: Juan Pellico, Irene Fernández-Barahona, Marina Benito, Ángel Gaitán-Simón, Lucía Gutiérrez, Jesús Ruiz-Cabello, Fernando Herranz , Unambiguous detection of atherosclerosis using bioorthogonal nanomaterials. Nano (2019), https://doi.org/10.1016/j.nano.2018.12.015

Unambiguous detection of atherosclerosis using bioorthogonal nanomaterials

Juan Pellico[a] PhD, Irene Fernández-Barahona[a,d] MSc, Marina Benito[b] PhD, Ángel Gaitán-Simón[c,d] MSc, Lucía Gutiérrez[e] PhD, Jesús Ruiz-Cabello[c,d] PhD and Fernando Herranz[a,f] PhD*

[a] Centro Nacional de Investigaciones Cardiovasculares Carlos III (CNIC) and CIBERES. C/ Melchor Fernández-Almagro 3. 28029 Madrid. Spain.
[b] Hospital Nacional de Paraplejicos de Toledo. 45071 Toledo, Spain.
[c] CIC biomaGUNE, Paseo de Miramón 182, 20014 Donostia - San Sebastián, Spain; Ikerbasque, Basque Foundation for Science, 48013 Bilbao, Spain;
[d] Universidad Complutense de Madrid and Centro de Investigación Biomédica en Red de Enfermedades Respiratorias (CIBERES). 28029 Madrid. Spain
[e] Departamento de Química Analítica, Instituto de Nanociencia de Aragón, Universidad de Zaragoza, Instituto de Ciencia de Materiales de Aragón (ICMA/CSIC) y CIBER-BBN. 50018 Zaragoza, Spain
[f] Instituto de Química Médica, Consejo Superior de Investigaciones Científicas (CSIC). C/ Juan de la Cierva 3. 28006 Madrid. Spain

word count abstract: 148
complete manuscript word count: 4070
number of references: 37
number of figures/tables: 6/0

Corresponding author: Dr. Fernando Herranz

Fundación Centro Nacional de Investigaciones Cardiovasculares (CNIC) and CIBER Enfermedades Respiratorias (CIBERES). Melchor Fernández Almagro, 3. 28029 Madrid, Spain
E-mail: fherranz@cnic.es

Confict of interest
The authors declare no conflicts of interest.

Funding sources
This work was funded by the Spanish Ministry for Economy and Competitiveness (MEyC) (grant number: SAF2016-79593-P) and Carlos III Health Institute (grant number: DTS16/00059). L.G. was funded by Ramon y Cajal grant (RYC-2014-15512).

Abstract

The importance of atherosclerosis is driving research to create improved diagnostic tools based on molecular imaging. Pretargeted imaging is the use of bioorthogonal probes that selectively accumulate upon reaction with a pre-modified biomolecule *in vivo*. To date, this very promising approach has not been applied to atherosclerosis. Neither has been the use of a single nano-radiomaterial for PET / T_1-MR imaging of atherosclerosis. Here, we synthesized bioorthogonal nano-radiomaterials for *in vivo* pretargeted molecular imaging in a mouse model of atherosclerosis. Based on tetrazine-ligation, these functionalized ^{68}Ga iron oxide nano-radiomaterials provide simultaneous PET and T_1-MRI signals and selectively accumulate in atherosclerotic plaques in mice sequentially injected with trans-cyclooctene-modified antibodies against oxidized LDL followed by the hybrid nano-radiomaterial. Our results demonstrate the ability of this approach to unambiguously detect atherosclerosis. Furthermore, we show the first example of how hybrid imaging can be used for pretargeted bioorthogonal molecular imaging with nanomaterials.

Keywords: Nano-radiomaterials, atherosclerosis, molecular imaging, iron oxide, gallium-68

Background

Atherosclerosis is a complex chronic inflammatory disease of the blood vessel wall in which plaques build up inside the arteries. The generation of oxidized low-density lipoprotein (oxLDL) plays a key role in the initiation, progression and destabilization of atherosclerotic lesions.[1] OxLDL has therefore been widely used as a target for molecular imaging of atherosclerosis. OxLDL is an important target not only due to its role in plaque pathobiology, but also because it is a possible marker of plaque vulnerability. Molecular imaging studies have focused on antibody-labeled magnetic resonance contrasts[2,3] and more recently on fluorescence.[4,5] In the field of nuclear imaging, there are a few examples of single-photon emission computed tomography (SPECT) [6–8] and a recent study using positron emission tomography.[9] The methodology in all these studies share the need to match the lengthy biodistribution of the different antibodies *in vivo* by using long half-life isotopes, such as ^{125}I ($t_{1/2}$ = 59 days) or ^{64}Cu ($t_{1/2}$ = 16 hours).

The development of probes for hybrid molecular imaging is particularly appealing for the early diagnosis and characterization of complex diseases like atherosclerosis. The combined use of positron emission tomography (PET) and magnetic resonance imaging (MRI) technology can provide combined structural and functional information, and this approach is beginning to show its potential, particularly in the cardiovascular area.[10,11] There is a growing number of contributions where atherosclerosis is characterized by hybrid PET/MR imaging. This is normally done by using a PET radiotracer and, after radioactive decay, carrying out the MRI experiments without any contrast agent,[12–14] or by separated PET and T_2-weigthed MRI experiments by the consecutive injection of two different probes,[15] or one surface-functionalized probe.[16] To our knowledge, the characterization of atherosclerosis with one probe for hybrid PET/T_1-MRI, in one

experiment, has not been done before. We recently developed a new kind of nano-radiomaterial in which short half-life ^{68}Ga isotopes are incorporated in the core of extremely small iron oxide particles, combining the size-dependent properties of nanotechnology with the unparalleled sensitivity of nuclear imaging techniques. This nano-radiomaterial (NRM) provides simultaneous signals for PET and T_1-MRI.[17,18] Bioorthogonal chemistry enables the selective conjugation of two compounds in the challenging *in vivo* environment. Since the ground-breaking work that initiated the use of this type of chemistry for biomedical applications, the field has expanded tremendously.[19–21]

Bioorthogonal or pretargeted molecular imaging is based on the complementary labelling of the biomolecule (typically an antibody) and the probe; after injection of the biomolecule, the tracer is administered and selectively accumulates at the site of the bioorthogonal reaction. This type of chemistry has many advantages in molecular imaging and is particularly appealing since it allows the use of short half-life isotopes to detect biomolecules with long biodistribution times.[22–24] This approach has already been applied to the characterization of cancer, using small chelators such as tracers,[25–27] antibodies,[28] or nanoparticles.[29–31] Among reactions showing bioorthogonal features, tetrazine ligation is probably the best suited for *in vivo* imaging. The extremely rapid reaction between *trans*-cyclooctene (TCO) and tetrazine (TZ) derivatives and the variety of compounds available make this reaction the first choice for many applications.

Methods

Antibody functionalization with trans- cyclooctene (Ab-TCO). E-06 antibody (200 µg) is added to an Eppendorf tube and volume adjusted with PBS 1X to a final volume of 0.5 ml. The pH of the solution was adjusted to 8.9-9.1 with 90 µl of Na_2CO_3 0.1 M. Then, 10 µl of TCO-NHS (1 $mg \cdot ml^{-1}$) were added and the reaction was kept at room temperature for 60 min in the vortex. Afterwards, the reaction was purified by ultra-filtration through 100 KDa cut off filters and dissolved in PBS 1X to reach 0.5 ml.

Synthesis of ^{68}Ga-NRM. $FeCl_3$ x 6 H_2O (75 mg, 0.28 mmol), citric acid trisodium salt (80 mg, 0.27 mmol) and 1280 MBq of $^{68}GaCl_3$ in HCl (0.05 M, 4 mL) were dissolved in water (5 mL) in a microwave-adapted flask, followed by addition of hydrazine hydrate (55%, 1 mL). The solution was ramped to 100°C over 54 s and held at this temperature for 10 minutes (240 W) in a Monowave 300 microwave reactor equipped with an internal temperature probe and an external IR probe (Anton Paar, GmbH73760, Ostfildern-Scharnhausen, Germany). The reaction mixture was then cooled to 60°C and the ^{68}Ga-NRM product was purified by passing the mixture through a PD-10 column to eliminate excess small reagents, including all unincorporated radiotracer. This purification process provided 9 mL of ^{68}Ga-NRM with a total activity of 781 MBq (measured 40 minutes after starting the reaction), a radiolabeling yield of 92%.

Synthesis of ^{68}Ga-NRM-TZ. To 650 MBq of ^{68}Ga-NRM (2.25 mL) were added 0.07 mmol of N-(3-dimethylaminopropyl)-N′-ethylcarbodiimide hydrochloride (EDC) and 0.075 mmol of N-hydroxysulfosuccinimide sodium salt (Sulfo-NHS). The solution was stirred for 30 min at room temperature (r.t.) and then ultracentrifuged at 10350 x g

through Amicon 30 kDa centrifugal filters for 4 min to remove excess reagents. The nanoparticles were resuspended in 1.5 mL of HEPES buffer 0.5 M, pH = 8, and 1 mg of Benzylamino tetrazine hydrochloride dissolved in 50 µL DMSO was added to the solution. The mixture was maintained at r.T. for 60 min with stirring. Finally, another ultrafiltration step was performed to eliminate unreacted tetrazine. The nanoparticles were resuspended in saline solution, yielding 188 MBq (Measured 120 minutes after starting reaction) of ^{68}Ga-NRM-TZ, a radiolabeling yield of 98.9%.

Analysis of serum. Blood samples were centrifuged at 10350 x g at 4ºC for 7 minutes to separate the serum for analysis.

Quantification TCO in Ab. To calculate the amount of TCO in E-06 Antibody after conjugation, reaction with fluorescent probe Cy3 Tetrazine (Click chemistry tools) was used. First, calibration curve was made at different concentrations of Cy3 Tetrazine: 100, 50, 10, 8, 6, 4, 2, 0.5 and 0.1 µM. Fluorescence signal was measured at λ = 570 nm. Then, 0.055 nmoles (50 µg) of the conjugate antibody-TCO dissolved in 100 µL of normal saline were mixed with Cy3-Tetrazine to give a final concentration of 200 µM. The final solution was vortexed for 2 hours at r.t. Afterwards, sample was purified by ultrafiltration with Amicon® 100K. Final product was resuspended in saline solution and the fluorescence signal was measured at λ = 570 nm.

Quantification TZ in ^{68}Ga-NRM-TZ. To calculate the amount of TZ per NRM after conjugation, fluorescent probe Cy5 TCO (Click chemistry tools) was used. To start with, a calibration curve was worked out measuring fluorescence signal of different TCO Cy5 concentrations (50, 10, 8, 6, 4, 2, 0.5 and 0.1 µM) at λ = 725 nm. Then, 250

µl (0.858 mg·ml^{-1} Fe) of ^{68}Ga-NRM-TZ dissolved in saline solution were mixed with Cy5 TCO to reach a final concentration of 300 µM. Resulting solution was vortexed for 6 hours at r.t. Once this step was completed, sample was purified by ultrafiltration with Amicon® 100K. Final product was resuspended in saline solution and fluorescence signal measured at λ = 725 nm.

In vitro bioorthogonal reaction. Ox-Phospholipid Snooper was first blocked using 10 mL TBS + 3% BSA for 1 hour at room temperature under gentle shaking. Once this step was completed, blocking solution was removed and 2 µg of Ab-TCO were added to the membrane in 10 mL TBS + 1% BSA and incubated for 1 hour at room temperature under gentle shaking. After this, antibody solution was discarded and membrane was washed three times with TBS + 3% BSA for 10 minutes. 200µl of NRM-TZ were added in 10 ml TBS + 1% BSA and incubated at room temperature for 1 hour under gentle shaking. After this, solution was discarded and membrane was washed three times with TBS + 3% BSA for 10 minutes. NRM accumulation was studied by naked-eye.

Animals and ethics. All animal experiments conducted in this work were approved by the ethics and animal welfare committee at CNIC and were developed according to the Spanish and UE legislation. Experimental protocol approved by Madrid regional government, PROEX 277/16.

Results

Synthesis and characterization of the nano-radiomaterial.

The general hybrid approach followed in this study is summarized in Figure 1. We first covalently attached the TCO moiety to E-06, a naturally occurring mouse monoclonal IgM antibody (Ab) targeting oxidized LDL, oxidized HDL, and proteins covalently modified by oxidized phospholipids. The pentameric structure of the E-06 Ab presents

plenty of accessible lysines to attach TCO (highlighted in blue in the IgM structure (Figure 1a). TCO is one of the most used molecules for bioorthogonal reactions because of its rapid reaction rate with TZ derivatives. The Ab was reacted with TCO N-hydroxisuccinimidyl ester and purified by ultrafiltration.

We quantified the number of TCO molecules per Ab by reacting the Ab-TCO with fluorescently tagged tetrazine (TZ-Cy3). After the *in vitro* bioorthogonal reaction and purification, the Ab showed quite a strong fluorescent signal (Figure 2a), indicating successful tetrazine ligation. Using this signal, we determined that approximately 48 TCO molecules were bound per Ab molecule (Figure S1), which is optimum for this type of *in vivo* chemistry[32]. In the second step, we synthesized a new ^{68}Ga-based nano-radiomaterial (^{68}Ga-NRM). We recently demonstrated the use of this hybrid nano-radiotracer for PET / MR tumor characterization *in vivo,*[17] and for the *in vivo* detection of neutrophils.[18]. Here, we produced a modified version, replacing the dextran coating with citrate molecules. The core consists of extremely small iron oxide nanoparticles doped with ^{68}Ga. NRM synthesis was carried out very rapidly in a microwave oven,[18] taking only 15 minutes to obtain the pure, ready-to-use sample. ^{68}Ga-NRM were purified by gel filtration.

Radioactive elution profile shows a large peak due to the ^{68}Ga incorporated in the core of the particles and a small peak due to free ^{68}Ga (Figure 2b). We next incorporated the tetrazine moiety to the ^{68}Ga-NRM surface through amide formation between benzylamino-tetrazine and the carboxylic acid groups in citrate (^{68}Ga-NRM-TZ, Figure 1b). Radioactive labelling stability was confirmed by incubation with mouse serum at 37ºC and then ultrafiltration. Data indicates that all the activity remains within the NRM, both for ^{68}Ga-NRM and ^{68}Ga-NRM-TZ, with no measurable activity in the filtrate (Figure 2c). Radiochemical purity of ^{68}Ga-NMR-TZ was also confirmed by size

exclusion HPLC analysis (Figure S2) showing the same elution time for the radioactive signal and the UV channel with absence of radioactive signal for free $^{68}Ga^{3+}$. The FTIR spectrum for unmodified ^{68}Ga-NRM showed the typical bands for citrate-coated iron oxide nanomaterials at 1551 cm^{-1}, 1374 cm^{-1}, and 1073 cm^{-1} (Figure 2d). After tetrazine conjugation, the ^{68}Ga-NRM-TZ spectrum showed 2 new bands due to the tetrazine ring, at 1156 cm^{-1} and 1030 cm^{-1}.[33] Further analysis by zeta potential measurements showed that tetrazine incorporation changed the surface charge from a mean value of -33 mV for ^{68}Ga-NRM to -25 mV for ^{68}Ga-NRM-TZ (N=3) due to the reduction in the number of free carboxylate groups (Figure 2e).

We next tested the presence and reactivity of TZ on the surface of the modified ^{68}Ga-NRM by *in vitro* bioorthogonal reaction with a commercial dye-labelled TCO (TCO-Cy5). This allowed us to confirm successful TZ conjugation and reactivity and to quantify the amount of conjugated TZ in the ^{68}Ga-NRM-TZ. The fluorescence spectrum after purification clearly shows the fluorescence signal from the Cy5 dye, whereas there is no signal from the initial ^{68}Ga-NRM-TZ used as control for the *in vitro* bioorthogonal incubation (Figure 2f, Figure S3).

To optimize TZ incorporation, we tested 4 benzylamino-tetrazine concentrations in the amidation reaction, quantifying amount of incorporated TZ in each reaction from the fluorescent signal (Figure 2g). TZ saturation was obtained with the addition of 15 µmol of benzylamino-tetrazine. We wanted a nano-radiomaterial able to undergo the bioorthogonal reaction while maintaining as far as possible the physicochemical properties of the original ^{68}Ga-NRM, and therefore selected reaction conditions resulting in a tracer incorporating 675 nmol of TZ per mmol Fe (Figure 1b).

To evaluate the colloidal properties of the samples we measured hydrodynamic size by dynamic light scattering. Hydrodynamic size was similar and extremely low in both

samples, measuring 14.7 ± 2.8 nm for ^{68}Ga-NRM (PDI 0.23 ± 0.02) and 15.5 ± 1.7 nm for ^{68}Ga-NRM-TZ (PDI 0.26 ± 0.04). Reproducibility was remarkable, with mean hydrodynamic size showing a very narrow distribution over five independent syntheses (Figure 2h). STEM-HAADF analysis determined a mean core size of 2.9 ± 0.9 nm for ^{68}Ga-NRM (Figure 2i) and 2.8 ± 0.6 nm for ^{68}Ga-NRM -TZ (Figure 2j, Figure S4). The size analyses thus show that, under the selected conditions, TZ conjugation does not alter the size, shape, or aggregation state of the citrate-coated nano-radiomaterial. The difference between core size and hydrodynamic size is due to the very thick organic coating in both samples (Figure S5 in the ESM).

A key feature of this ^{68}Ga-NRM is its simultaneous provision of hot spot (positive) signals for PET and MRI. To confirm conservation of this property after TZ conjugation, we measured the relaxivity values for ^{68}Ga-NRM and ^{68}Ga-NRM-TZ at 37ºC and a 1.5 T field strength (Figure 2k). Functionalization with TZ did not alter relaxometric behavior of ^{68}Ga-NRM. ^{68}Ga-NRM-TZ had a large r_1 value of 7.1 $mM^{-1}\cdot s^{-1}$. This figure is larger than those for the clinically approved Gd-based complexes Magnevist© and Omniscan©, which have r_1 values of 4.1 $mM^{-1}\cdot s^{-1}$ at 1.5 T and 3.9 $mM^{-1}\cdot s^{-1}$ at 1.0 T, respectively. The relaxivity value for ^{68}Ga-NRM-TZ results in a very low r_2/r_1 ratio of 2.5 that underlies the positive contrast ability of this bioorthogonal ^{68}Ga-NRM. This was confirmed with phantom images of ^{68}Ga-NRM-TZ, showing a clearly increased positive contrast in MRI and a simultaneous increase in the PET signal due to the core-doped ^{68}Ga (Figure 2l).

To study the ^{68}Ga-NRM-TZ–*trans*-cyclooctene reaction kinetics, we reacted ^{68}Ga-NRM-TZ with different amounts of fluorescent TCO-Cy5 and calculated the pseudo first order rate constant (Figure 2m). As expected, the plots reveal fast reaction rates, with reactions completed within 15 to 20 minutes. Plotting these constants against the

molar concentration and linear fitting of the slope revealed a second order rate constant of 301 ± 27 $M^{-1} \cdot s^{-1}$ (Figure S6 in the ESM). This value is in the normal range for an inverse demand Diels-Alder reaction and should guarantee a sufficiently fast reaction for *in vivo* imaging.[34]

We studied the specificity of our Ab-TCO and demonstrated the bioorthogonal reaction *in vitro* by using commercial oxidized phospholipid snoopers. These consist of 12 different lipid species spotted individually on a paper support, each spot containing 1 µg of the pure lipid.[35] E06 antibody recognizes only the phosphocholine headgroup of oxidized phospholipid that is present in oxidized LDL, oxPAPC in the snooper. Therefore, if our Ab-TCO had the same reactivity as E06 we should only observe signal in the spot corresponding to that antigen (oxPAPC). We first incubated the snooper with the Ab-TCO, after that, we washed it and further incubated with our NRM-TZ. If the bioorthogonal reaction was happening we should detect the correct spot (oxPAPC) but because of the iron oxide accumulation. Results (Figure S7) confirm both the expected specificity of the antibody, there is only signal at the oxPAPC spot; and the selective reaction with the NRM-TZ, there is no accumulation of nanoparticles anywhere else. Because of the iron oxide nanoparticles color the accumulation can be directly observed by naked eye.

Biodistribution, clearance and in vivo toxicity.

We studied the biodistribution, clearance and *in vivo* toxicity of the probe, ^{68}Ga-NRM-TZ in the same conditions designed for the *in vivo* imaging experiments. The ^{68}Ga-NRM-TZ (1.7 nmol TZ, 12 MBq, 1.4 mg Fe/mL) was intravenously injected in ApoE$^{-/-}$ mice (42 weeks old, 25 weeks on a high fat diet; HFD). Ab-TCO (55 pmol) had been previously (24 h) injected. Three hours post-injection of ^{68}Ga-NRM-TZ animals were sacrificed, organs harvested and the radioactive doses measured in a gammacounter.

Biodistribution results (Figure 3a) show a large accumulation in spleen and liver, typical of these NRM and of nanoparticles with this size [18]. Importantly, the percentage of dose is very large in the aorta, almost the same as in the liver, suggesting a successful accumulation with the pretargeted approach. The rest of the organs show very low levels of radioactivity, as expected.

For the clearance studies the same conditions were followed but including two groups of ApoE$^{-/-}$ mice (42 weeks old, 25 weeks on a high fat diet; HFD) for comparison. In both groups, we injected the ^{68}Ga-NRM-TZ (1.7 nmol TZ, 12 MBq, 1.4 mg Fe/mL). To the first group Ab-TCO (55 pmol) had been injected, 24 h before, while the second group was free of antibody. This way we could investigate if the pretargeted approach had any effect on the clearance of the NRM from the animals. Dynamic PET was used to monitor the activity in the whole body at different time points; 11 time points, from 5 min to 90 min. Results, reported as mean standardized uptake values (SUV), show clearance from circulation (Figure 3b) and concomitant accumulation in liver (Figure 3c), spleen (Figure 3d) and, to a lesser extent, in the bladder (Figure 3e) after approximately 60 minutes of injection of NRM. Clearly there is no difference between the two groups of animals, i.e. the injection of the Ab-TCO does not change the clearance profile of the NRM.

The long-term *in vivo* effects of the ^{68}Ga-NRM-TZ injection was studied in ApoE$^{-/-}$ mice. The serum levels for iron, total iron binding capacity (TIBC), alanine aminotransferase (ALT), aspartate aminotransferase (ALT) and alkaline phosphatase (AKP) were monitored 1 day, 3 days, 10 days and 18 days post-injection of the NRM or saline as control. As figure 4a shows, iron levels in serum don't change in comparison to baseline values or saline injection. This is most likely due to the low concentration of

iron injected and its rapid elimination. Since the most important elimination organ is the liver we focused in the analysis of several indicators of liver function.

TIBC represent the amount of iron that would be present in circulation should all the transferrin be saturated. Since transferrin is produced in the liver, TIBC is used as an indirect measurement of liver function. Similarly to iron levels, TIBC does not change compared to saline injection or baseline levels (Figure 4b). To complete the assessment of liver function after the injection of the NRM, the levels of ALT, AST and AKP were measured. In the case of ALT (Figure 4c) and AST (Figure 4d) the values slightly increase 10 days after the injection, both for saline and NRM injections, discarding any deleterious effect by the NRM. This change is normal considering that liver function in ApoE$^{-/-}$ mice is affected. In fact, ApoE$^{-/-}$ are considered also a model for non-alcoholic steatohepatitis.[36,37] Finally, data for AKP don't show any difference between the injection of our NRM or saline (Figure 4e). Altogether, clearance and toxicity data indicate that the two steps protocol does not affect the normal clearance of the probe, the typical for nanoparticles this size. Furthermore, the injection of the ^{68}Ga-NRM-TZ does not elicit any deleterious effect in the animals, even considering that the main accumulation organ is the liver and that ApoE$^{-/-}$ can suffer from altered liver function.

Pretargeted hybrid detection of atherosclerosis.

Having completed the characterization of the Ab-TCO and ^{68}Ga-NRM-TZ components of the pretargeted approach, we proceeded to the *in vivo* imaging, using the strategy depicted in Figure 1c. In order to have a complete study we used the following 5 different conditions (Figure 5):

a) Full pretargeted approach (55 pmol of Ab-TCO + ^{68}Ga-NRM-TZ) on atherosclerotic mice on high fat diet (42 weeks old, 25 weeks on a high fat diet, ApoE$^{-/-HFD}$)

b) Full pretargeted approach on control C57BL/6 mice (42 weeks old).

c) Full pretargeted approach on ApoE$^{-/-}$ in normal (chow) diet (42 weeks old, ApoE$^{-/-chow}$).

d) Pretargeted approach using control particles (^{68}Ga-NRM) without tetrazine on ApoE$^{-/-HFD}$

e) Blocking experiment where, prior to the full pretargeted approach (55 pmol of Ab-TCO + ^{68}Ga-NRM-TZ), the Ab was intravenously injected to block most of the recognition sites.

Figure 5 shows a summary of the main findings after the PET/CT on these 5 conditions. Axial PET/CT images are all from the same anatomical region, the aortic arch (see also Figure S8 in the ESM). For condition a) PET/CT imaging of ApoE$^{-/-}$ mice 1 hour after ^{68}Ga-NRM-TZ injection revealed the unambiguous specific localization in several consecutive planes of the aortic arch (Figure 5a). In contrast, post ^{68}Ga-NRM-TZ injection images from control C57BL/6 and ApoE $^{-/-chow}$ mice showed no noticeable signal in the aortic arch or whole aorta (Fig 5b and 5c). For condition d) PET/CT signal was also absented from ApoE$^{-/-HFD}$ mice injected with unmodified ^{68}Ga-NRM (Figure 5d). Finally, in the blocking experiment, condition e), no signal was found.

Nano-radiomaterial biodistribution was studied with a gammacounter after the imaging experiment (Figure S9). Analysis of radioactivity in the aorta revealed a remarkably large uptake in ApoE$^{-/-HFD}$ mice (14.7 ± 2.7 %ID/g, N=4) compared to control conditions; b) 3.4 ± 1.5 %ID/g, N=3; c) 1.5 ± 0.5 %ID/g, N=3; d) 1.5 ± 0.3 %ID/g, N=3 and e) 2.0 ± 0.8 %ID/g, N=5.

These measurements confirm the clear uptake observed in the imaging experiments. It is especially noticeable the very large accumulation of signal in the pretargeted approach with an outstaning 14.7 % ID/g, confirming the specific accumulation of ^{68}Ga-NRM-TZ

due to the bioorthogonal reaction with E06-TCO antibody. Furthermore, the results for two of the control conditions are particularly important since they demonstrate that the large uptake in the aorta (in condition a) is due to the specificity of the biorthogonal reaction (no uptake in condition d) and the selective recognition of oxidized phospholipids by the antibody (no uptake in the blocking experiment, condition e). This clear *in vivo* signal is remarkable considering the small amount of injected Ab-TCO, providing clear evidence of the potential of this pretargeted approach with modified ^{68}Ga-NRM. The good relaxometric values of ^{68}Ga-NRM-TZ prompted us to check the ability of MRI to detect particle accumulation in the aorta. Given the poor sensitivity of MRI, monitoring the localization of iron oxide nanoparticles using their T_1 properties is non-trivial, especially at high magnetic fields. We recently demonstrated the feasibility of this approach,[17] but in the present study we needed to take into account the extremely low concentration range used. Because of this limitation, we investigated the potential of MRI by *ex vivo* analysis of aortas from ApoE$^{-/-}$ mice injected with ^{68}Ga-NRM or ^{68}Ga-NRM-TZ (Figure 6). We performed a double-blind experiment in which the researchers injecting the tracers and extracting aortas were not involved in MRI acquisition and data analysis, and researchers analyzing the data didn't know *a priori* which animals were control or experimental. This approach allowed us to successfully distinguish between animals injected with ^{68}Ga-NRM and those injected with ^{68}Ga-NRM-TZ solely on the basis of imaging results. Clear hyperintense areas were evident in lesions, both in the axial view and in the 3D representation of the aorta (Figure 6c). Pseudocolored images show clear hypertintense areas in the lesion after the injection of ^{68}Ga-NRM-TZ.

Discussion

The non-invasive diagnosis of atherosclerosis is a hot topic in nanomedicine and molecular imaging. Although many imaging probes have been studied, it is not easy to find one providing clear *in vivo* detection. Among the many targets present in the disease we focused in oxidized phospholipids, key compounds in the initiation and progression of atherosclerosis. In this study we have used combination of biorthogonal chemistry and nano-radiomaterials for the detection of the disease in animal models. The rationale of using pretargeted imaging is based on three factors: the use of short half-life radioisotopes, the higher selectivity of the radiotracer, thus avoiding healthy tissue, and the rapid excretion of the radiotracer.[21] With this aim we functionalized a commercially available antibody with TCO by amide formation. Quantification of this group showed and optimal value of 48 TCO molecules per IgM. The second component of the pretargeted imaging studied consisted on our ^{68}Ga core-doped iron oxide nanoparticles, functionalized with TZ and, this way, ready for the biorthogonal reaction with the modified antibody. These NRM present excellent colloidal stability, stable radiolabeling and provide good T_1-based signal in MRI as we have shown. Compared with traditional pretargeted imaging, the most remarkable features of our approach are the use of short half-life radioisotopes, the unambiguous detection of atherosclerosis with picomolar concentrations of the Ab and nanomolar concentrations of the NRM, and the use of hybrid PET/MR imaging to detect and structurally characterize the damaged tissue. These advances come at the cost of losing the rapid tracer excretion due to the size of the nanomaterial; however, this cost is more than compensated by the advantages, particularly in such a difficult field as atherosclerosis imaging. Proof of this is the important uptake detected in the aorta, with values difficult to see in the literature, key to this unambiguous detection of atherosclerosis. Furthermore, the large specific surface of these NRM makes them amenable to the incorporation of new moieties,

permitting new approaches, especially for therapy. The production of a new kind of bioorthogonal nano-radiomaterials through the synergistic combination of nanotechnology and radiochemistry shows for the first time that the range of applications of pretargeted imaging can be expanded to cardiovascular diseases and other *in vivo* imaging applications.

Acknowledgements

The CNIC is supported by the MEyC and the Pro-CNIC Foundation and is a SO-Center of Excellence (SEV-2015-0505).

References

(1) Miller, Y. I., Choi, S.-H., Wiesner, P., Fang, L., Harkewicz, R., Hartvigsen, K., Boullier, A., Gonen, A., Diehl, C. J., Que, X., Montano, E., Shaw, P. X., Tsimikas, S., Binder, C. J., and Witztum, J. L. (2011) Oxidation-specific epitopes are danger-associated molecular patterns recognized by pattern recognition receptors of innate immunity. *Circ. Res. 108*, 235–48.

(2) Briley-Saebo, K. C., Cho, Y. S., Shaw, P. X., Ryu, S. K., Mani, V., Dickson, S., Izadmehr, E., Green, S., Fayad, Z. A., and Tsimikas, S. (2011) Targeted iron oxide particles for in vivo magnetic resonance detection of atherosclerotic lesions with antibodies directed to oxidation-specific epitopes. *J. Am. Coll. Cardiol. 57*, 337–47.

(3) Briley-Saebo, K. C., Shaw, P. X., Mulder, W. J. M., Choi, S. H., Vucic, E., Aguinaldo, J. G. S., Witztum, J. L., Fuster, V., Tsimikas, S., and Fayad, Z. A. (2008) Targeted molecular probes for imaging atherosclerotic lesions with magnetic resonance using antibodies that recognize oxidation-specific epitopes. *Circulation 117*, 3206–3215.

(4) Lu, T., Wen, S., Cui, Y., Ju, S.-H., Li, K. C., and Teng, G.-J. (2014) Near-infrared fluorescence imaging of murine atherosclerosis using an oxidized low density lipoprotein-targeted fluorochrome. *Int. J. Cardiovasc. Imaging 30*, 221–31.

(5) Khamis, R. Y., Woollard, K. J., Hyde, G. D., Boyle, J. J., Bicknell, C., Chang, S.-H., Malik,

T. H., Hara, T., Mauskapf, A., Granger, D. W., Johnson, J. L., Ntziachristos, V., Matthews, P. M., Jaffer, F. A., and Haskard, D. O. (2016) Near Infrared Fluorescence (NIRF) Molecular Imaging of Oxidized LDL with an Autoantibody in Experimental Atherosclerosis. *Sci. Rep. 6*, 21785.

(6) Torzewski, M., Shaw, P. X., Han, K.-R., Shortal, B., Lackner, K. J., Witztum, J. L., Palinski, W., and Tsimikas, S. (2004) Reduced in vivo aortic uptake of radiolabeled oxidation-specific antibodies reflects changes in plaque composition consistent with plaque stabilization. *Arterioscler. Thromb. Vasc. Biol. 24*, 2307–12.

(7) Shaw, P. X., Hörkkö, S., Tsimikas, S., Chang, M. K., Palinski, W., Silverman, G. J., Chen, P. P., and Witztum, J. L. (2001) Human-derived anti-oxidized LDL autoantibody blocks uptake of oxidized LDL by macrophages and localizes to atherosclerotic lesions in vivo. *Arterioscler. Thromb. Vasc. Biol. 21*, 1333–9.

(8) Tsimikas, S., Shortal, B. P., Witztum, J. L., and Palinski, W. (2000) In vivo uptake of radiolabeled MDA2, an oxidation-specific monoclonal antibody, provides an accurate measure of atherosclerotic lesions rich in oxidized LDL and is highly sensitive to their regression. *Arterioscler. Thromb. Vasc. Biol. 20*, 689–97.

(9) Sasaki, T., Kobayashi, K., Kita, S., Kojima, K., Hirano, H., Shen, L., Takenaka, F., Kumon, H., and Matsuura, E. (2017) In vivo distribution of single chain variable fragment (scFv) against atherothrombotic oxidized LDL/β2-glycoprotein I complexes into atherosclerotic plaques of WHHL rabbits: Implication for clinical PET imaging. *Autoimmun. Rev. 16*, 159–167.

(10) Lau, J. M. C., Laforest, R., Nensa, F., Zheng, J., Gropler, R. J., and Woodard, P. K. (2017) Cardiac Applications of PET/MR Imaging. *Magn. Reson. Imaging Clin. N. Am. 25*, 325–333.

(11) Tarkin, J. M., Dweck, M. R., Evans, N. R., Takx, R. A. P., Brown, A. J., Tawakol, A., Fayad, Z. A., and Rudd, J. H. F. (2016) Imaging Atherosclerosis. *Circ. Res. 118*, 750–769.

(12) Keliher, E. J., Ye, Y.-X., Wojtkiewicz, G. R., Aguirre, A. D., Tricot, B., Senders, M. L., Groenen, H., Fay, F., Perez-Medina, C., Calcagno, C., Carlucci, G., Reiner, T., Sun, Y., Courties, G., Iwamoto, Y., Kim, H.-Y., Wang, C., Chen, J. W., Swirski, F. K., Wey, H.-Y., Hooker, J., Fayad, Z. A., Mulder, W. J. M., Weissleder, R., and Nahrendorf, M. (2017)

Polyglucose nanoparticles with renal elimination and macrophage avidity facilitate PET imaging in ischaemic heart disease. *Nat. Commun. 8*, 14064.

(13) Li, X., Heber, D., Leike, T., Beitzke, D., Lu, X., Zhang, X., Wei, Y., Mitterhauser, M., Wadsak, W., Kropf, S., Wester, H. J., Loewe, C., Hacker, M., and Haug, A. R. (2017) [68Ga]Pentixafor-PET/MRI for the detection of Chemokine receptor 4 expression in atherosclerotic plaques. *Eur. J. Nucl. Med. Mol. Imaging* 1–9.

(14) Nie, X., Laforest, R., Elvington, A., Randolph, G. J., Zheng, J., Voller, T., Abendschein, D. R., Lapi, S. E., and Woodard, P. K. (2016) PET/MRI of Hypoxic Atherosclerosis Using 64Cu-ATSM in a Rabbit Model. *J. Nucl. Med. 57*, 2006–2011.

(15) Millon, A., Dickson, S. D., Klink, A., Izquierdo-Garcia, D., Bini, J., Lancelot, E., Ballet, S., Robert, P., Mateo de Castro, J., Corot, C., and Fayad, Z. A. (2013) Monitoring plaque inflammation in atherosclerotic rabbits with an iron oxide (P904) and 18F-FDG using a combined PET/MR scanner. *Atherosclerosis 228*, 339–345.

(16) Sosnovik, D. E., Nahrendorf, M., Weissleder, R., Panizzi, P., Sosnovik, D. E., Aikawa, E., Libby, P., Swirski, F. K., and Weissleder, R. (2007) Molecular Magnetic Resonance Imaging in Cardiovascular Medicine. *Circulation 115*, 2076–2086.

(17) Pellico, J., Ruiz-Cabello, J., Saiz-Alía, M., del Rosario, G., Caja, S., Montoya, M., Fernández de Manuel, L., Morales, M. P., Gutiérrez, L., Galiana, B., Enríquez, J. A., and Herranz, F. (2016) Fast synthesis and bioconjugation of 68 Ga core-doped extremely small iron oxide nanoparticles for PET/MR imaging. *Contrast Media Mol. Imaging 11*, 203–210.

(18) Pellico, J., Lechuga-Vieco, A. V., Almarza, E., Hidalgo, A., Mesa-Nuñez, C., Fernández-Barahona, I., Quintana, J. A., Bueren, J., Enríquez, J. A., Ruiz-Cabello, J., and Herranz, F. (2017) In vivo imaging of lung inflammation with neutrophil-specific 68Ga nano-radiotracer. *Sci. Rep. 7*, 13242.

(19) Hashimoto, A., Suenaga, K., Gloter, A., Urita, K., Iijima, S., Prescher, J. A., Dube, D. H., and Bertozzi, C. R. (2004) Chemical remodelling of cell surfaces in living animals. *Nature 430*, 870–3.

(20) Prescher, J. A., and Bertozzi, C. R. (2005) Chemistry in living systems. *Nat. Chem. Biol. 1*,

13–21.

(21) Altai, M., Membreno, R., Cook, B., Tolmachev, V., and Zeglis, B. (2017) Pretargeted Imaging and Therapy. *J. Nucl. Med.* jnumed.117.189944.

(22) Carroll, L., Evans, H. L., Aboagye, E. O., and Spivey, A. C. (2013) Bioorthogonal chemistry for pre-targeted molecular imaging – progress and prospects. *Org. Biomol. Chem. 11*, 5772.

(23) Zeng, D., Zeglis, B. M., Lewis, J. S., and Anderson, C. J. (2013) The Growing Impact of Bioorthogonal Click Chemistry on the Development of Radiopharmaceuticals. *J. Nucl. Med. 54*, 829–832.

(24) Knight, J. C., and Cornelissen, B. (2014) Bioorthogonal chemistry: implications for pretargeted nuclear (PET/SPECT) imaging and therapy. *Am. J. Nucl. Med. Mol. Imaging 4*, 96–113.

(25) Rossin, R., Renart Verkerk, P., van den Bosch, S. M., Vulders, R. C. M., Verel, I., Lub, J., and Robillard, M. S. (2010) In Vivo Chemistry for Pretargeted Tumor Imaging in Live Mice. *Angew. Chemie Int. Ed. 49*, 3375–3378.

(26) Denk, C., Svatunek, D., Mairinger, S., Stanek, J., Filip, T., Matscheko, D., Kuntner, C., Wanek, T., and Mikula, H. (2016) Design, Synthesis, and Evaluation of a Low-Molecular-Weight 11C-Labeled Tetrazine for Pretargeted PET Imaging Applying Bioorthogonal in Vivo Click Chemistry. *Bioconjug. Chem. 27*, 1707–1712.

(27) Adumeau, P., Carnazza, K. E., Brand, C., Carlin, S. D., Reiner, T., Agnew, B. J., Lewis, J. S., and Zeglis, B. M. (2016) A pretargeted approach for the multimodal PET/NIRF imaging of colorectal cancer. *Theranostics 6*, 2267–2277.

(28) Cook, B. E., Adumeau, P., Membreno, R., Carnazza, K. E., Brand, C., Reiner, T., Agnew, B. J., Lewis, J. S., and Zeglis, B. M. (2016) Pretargeted PET Imaging Using a Site-Specifically Labeled Immunoconjugate. *Bioconjug. Chem. 27*, 1789–1795.

(29) Lee, S. B., Kim, H. L., Jeong, H. J., Lim, S. T., Sohn, M. H., and Kim, D. W. (2013) Mesoporous silica nanoparticle pretargeting for PET imaging based on a rapid bioorthogonal reaction in a living body. *Angew. Chemie - Int. Ed. 52*, 10549–10552.

(30) Lee, S., Koo, H., Na, J. H., Han, S. J., Min, H. S., Lee, S. J., Kim, S. H., Yun, S. H., Jeong, S. Y., Kwon, I. C., Choi, K., and Kim, K. (2014) Chemical tumor-targeting of nanoparticles based on metabolic glycoengineering and click chemistry. *ACS Nano 8*, 2048–2063.

(31) Hou, S., Choi, J. S., Garcia, M. A., Xing, Y., Chen, K. K.-J. J., Chen, Y.-M. M., Jiang, Z. K., Ro, T., Wu, L., Stout, D. B., Tomlinson, J. S., Wang, H., Chen, K. K.-J. J., Tseng, H.-R. R., and Lin, W.-Y. Y. (2016) Pretargeted Positron Emission Tomography Imaging That Employs Supramolecular Nanoparticles with in Vivo Bioorthogonal Chemistry. *ACS Nano 10*, 1417–1424.

(32) Haun, J. B., Devaraj, N. K., Hilderbrand, S. A., Lee, H., and Weissleder, R. (2010) Bioorthogonal chemistry amplifies nanoparticle binding and enhances the sensitivity of cell detection. *Nat. Nanotechnol. 5*, 660–665.

(33) Spencer, G. H., Cross, P. C., and Wiberg, K. B. (1961) s-Tetrazine. II. Infrared Spectra. *J. Chem. Phys. 35*, 1939–1945.

(34) Devaraj, N. K., Upadhyay, R., Haun, J. B., Hilderbrand, S. A., and Weissleder, R. (2009) SUPP INFO Fast and Sensitive Pretargeted Labeling of Cancer Cells through a Tetrazine/ trans -Cyclooctene Cycloaddition. *Angew. Chemie Int. Ed. 48*, 7013–7016.

(35) https://www.sigmaaldrich.com/content/dam/sigma-aldrich/docs/Avanti/Bulletin/1/330501bul.pdf.

(36) Tous, M., Ferré, N., Camps, J., Riu, F., and Joven, J. (2005) Feeding apolipoprotein E-knockout mice with cholesterol and fat enriched diets may be a model of non-alcoholic steatohepatitis. *Mol. Cell. Biochem. 268*, 53–8.

(37) Jeon, S., Park, Y.-J., and Kwon, Y. H. (2014) Genistein alleviates the development of nonalcoholic steatohepatitis in ApoE —/— mice fed a high-fat diet. *Mol. Nutr. Food Res. 58*, 830–841.

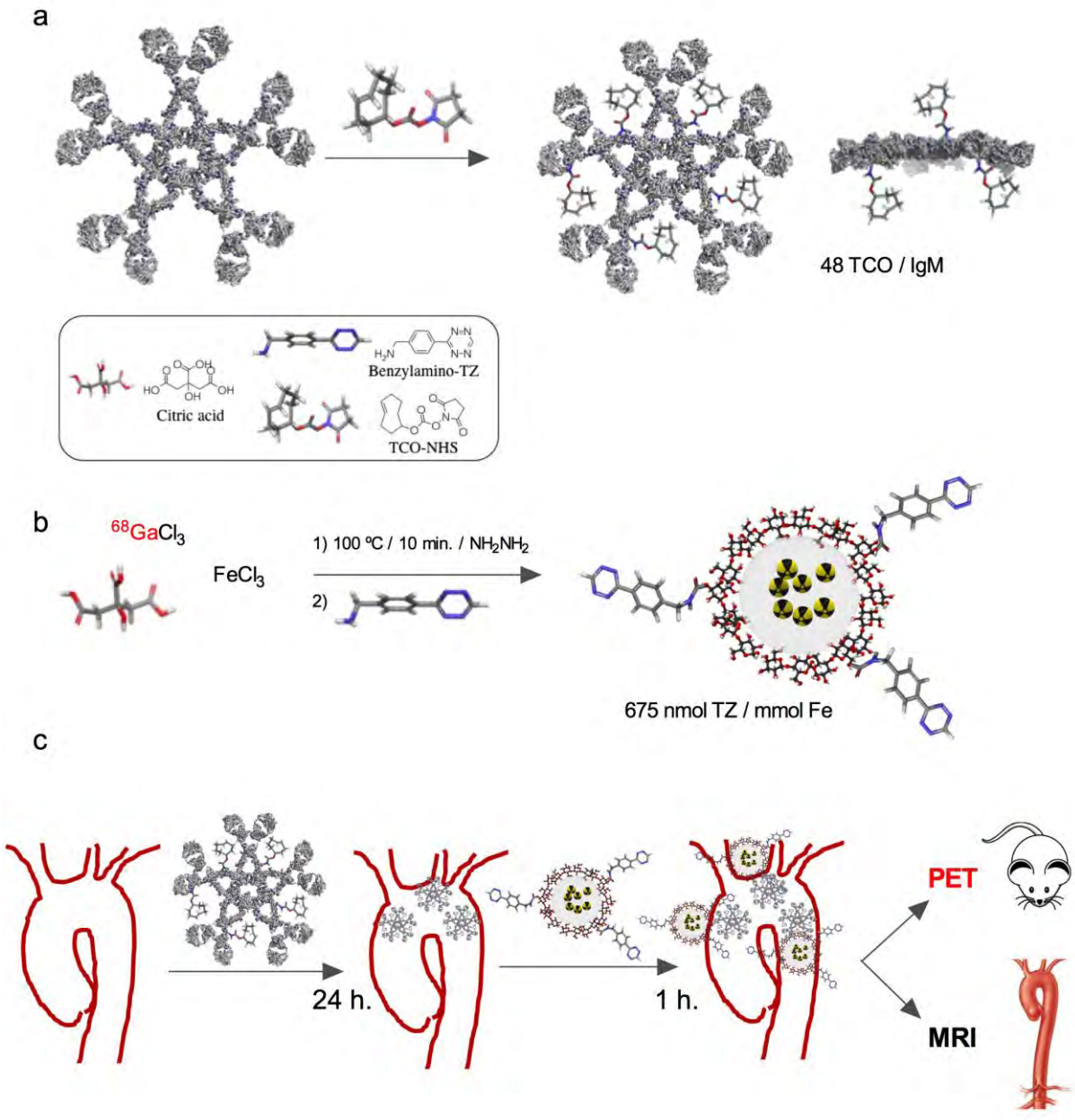

Figure 1. The approach followed in this study. a) IgM 3D structure and the conjugation of TCO molecules targeting primary amino groups in lysines (highlighted in blue in the structure, not to scale); b) Synthesis of ^{68}Ga core-doped iron oxide nano-radiomaterials (NRM) and their functionalization with a tetrazine derivative compound. c) Imaging protocol. Mice received injections of Ab-TCO followed 24 hours later by injection of ^{68}Ga-NRM-TZ. After 1 hour, *in vivo* PET scans were recorded of atherosclerotic lesions, and aortas were then excised and examined by *ex vivo* T_1-MRI to detect localized regions of NRM accumulation.

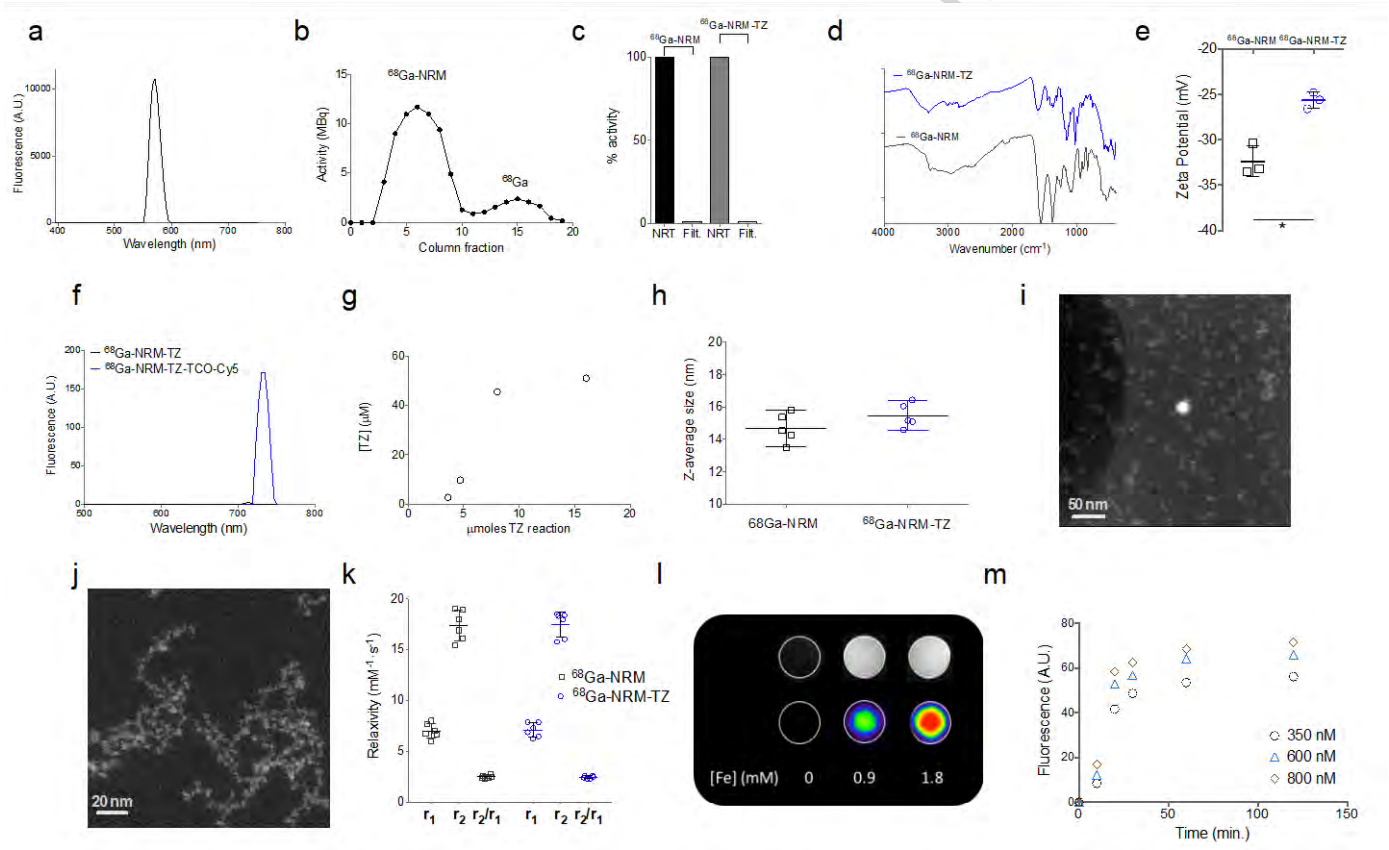

Figure 2. a) Fluorescence spectrum of Ab-TCO after bioorthogonal reaction with TZ-Cy3. b) gel filtration radio-chromatogram of the synthesized ^{68}Ga-NRM; c) percentage of the total activity measured in the particles and the filtrate after incubation with mouse serum at 37 ºC for 45 minutes, for ^{68}Ga-NRM and ^{68}Ga-NRM-TZ after ultracentrifugation; d) FTIR spectra for ^{68}Ga-NRM and ^{68}Ga-NRM-TZ; e) zeta potential values for ^{68}Ga-NRM and ^{68}Ga-NRM-TZ (statistical analysis by two-tailed *t*-test, error bars indicate s.d., N = 3; *, *P* 0.0138). f) fluorescence spectrum of ^{68}Ga-NRM-TZ before and after bioorthogonal reaction with TCO-Cy5; g) quantification of TZ molecules in ^{68}Ga-NRM-TZ versus the initial amount of benzylamino-tetrazine in the reaction with citrate molecules; h) hydrodynamic size values for five independent syntheses of ^{68}Ga-NRM and ^{68}Ga-NRM-TZ; scatter dot plot with 95% CI. i) STEM-HAADF for ^{68}Ga-NRM; scale bar, 50 nm. j) STEM-HAADF for ^{68}Ga-NRM -TZ; scale bar, 20 nm. k) relaxivity values (r_1, r_2 and r_2/r_1) for ^{68}Ga-NRM and ^{68}Ga-NRM-TZ. l) image phantoms obtained at different iron concentrations of ^{68}Ga-NRM-TZ by MRI (top row) and PET

(bottom row) and m) reaction rates for ^{68}Ga-NRM-TZ cycloaddition to different concentrations of TCO-Cy5.

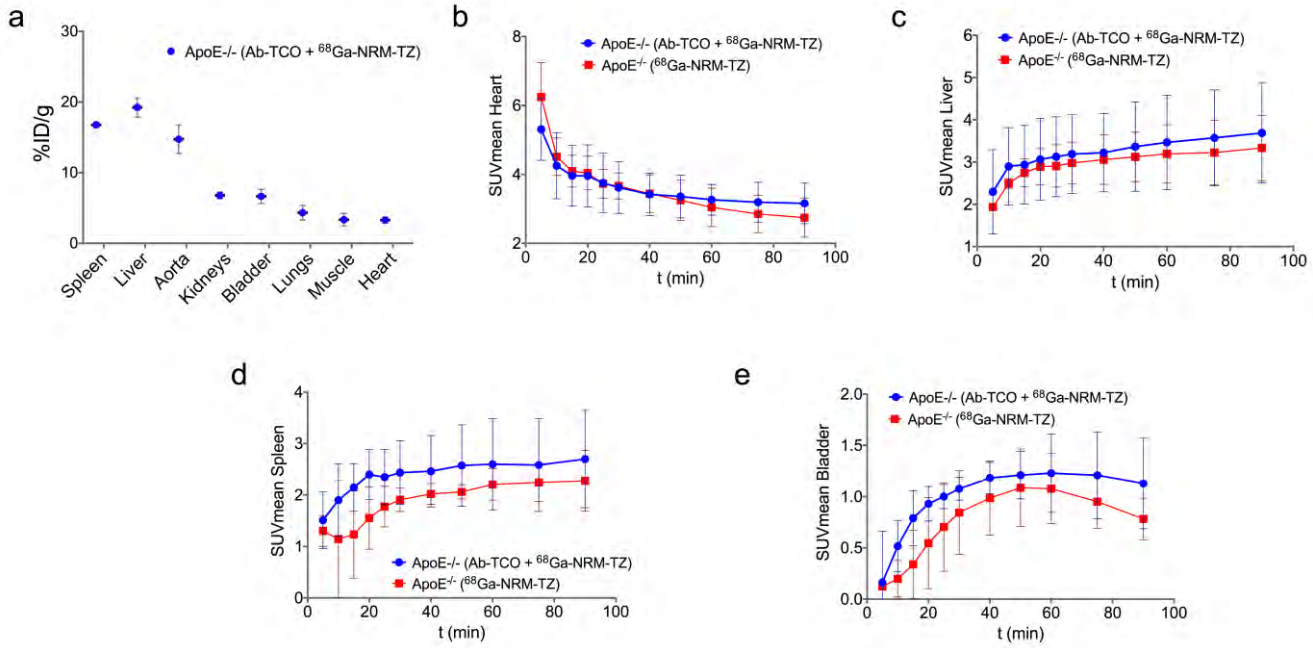

Figure 3. a) ^{68}Ga-NRM-TZ organ biodistribution expressed as the percentage injected dose per gram (%ID/g) in ApoE$^{-/-}$ mice (24 h before Ab-TCO was injected, N=5). Standardized uptake values from dynamic PET up to 120 minutes post-injection of ^{68}Ga-NRM-TZ in b) heart; c) liver; d) spleen and e) bladder (N=3).

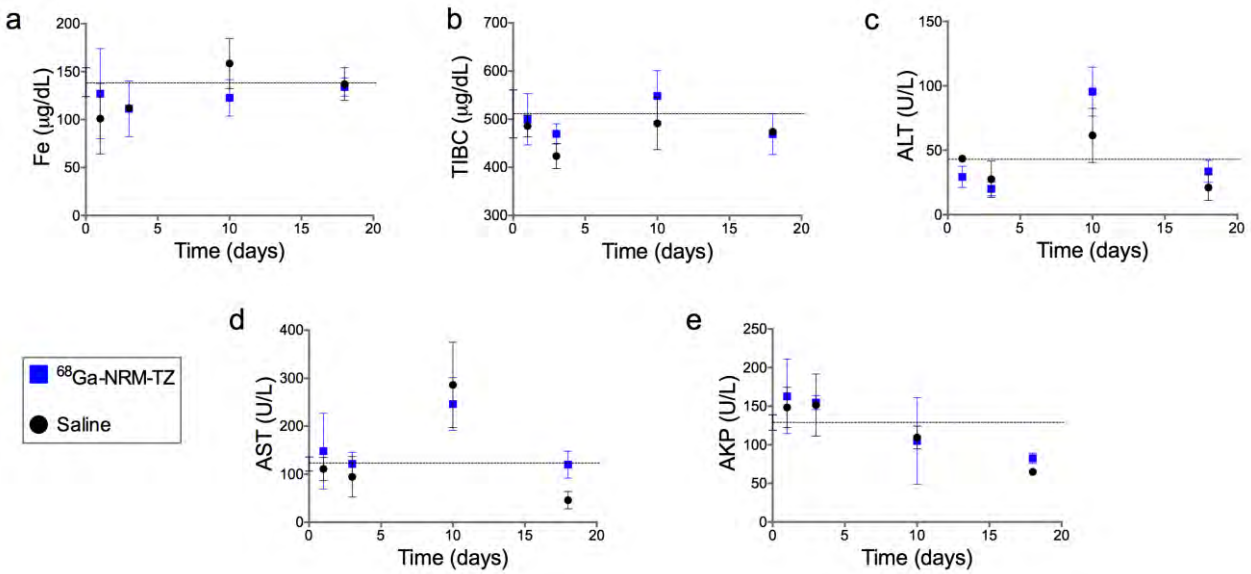

Figure 4. Serum levels in ApoE$^{-/-}$ mice after the injection of saline (N = 2) or ^{68}Ga-NRM-TZ (N = 4) for: a) iron; b) total iron binding capacity; c) alanine aminotransferase; d) aspartate aminotransferase and e) alkaline phosphatase. Dotted line indicates baseline levels.

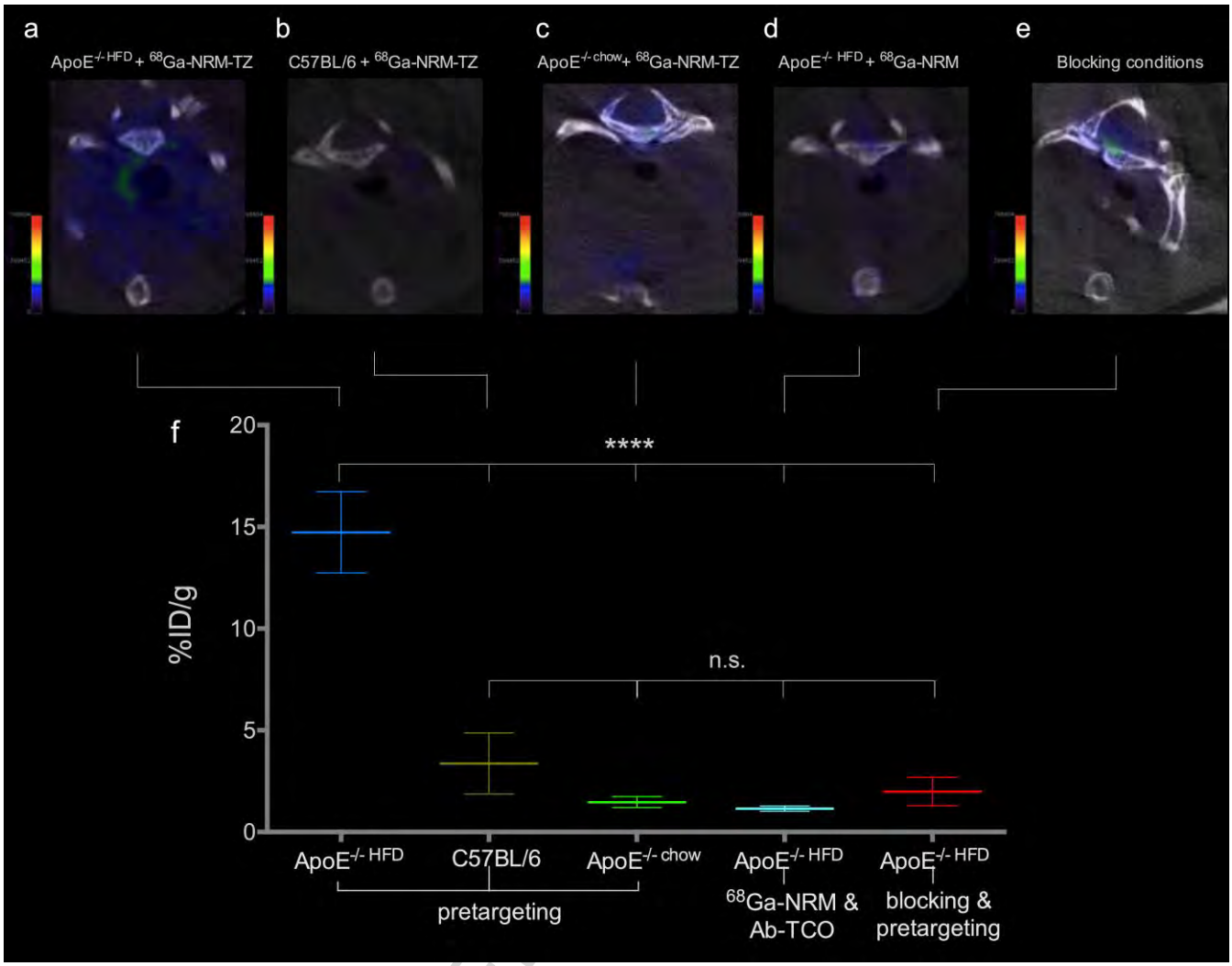

Figure 5. a-e), Axial PET/CT images taken 24 h post-injection of Ab-TCO and 1 h post-injection of nano-radiotracer: **a**, ApoE$^{-/-HFD}$ mice injected with ^{68}Ga-NRM-TZ; **b**, C57BL/6 mice injected with ^{68}Ga-NRM-TZ; **c**, ApoE$^{-/-chow}$ mice injected with ^{68}Ga-NRM-TZ; **d**, ApoE$^{-/-HFD}$ mice injected with ^{68}Ga-NRM and **e**, ApoE$^{-/-HFD}$ mice injected with Ab, prior to Ab-TCO, and ^{68}Ga-NRM-TZ. f) Radioactivity uptake in mice aortas for the five conditions, detected with a gamma counter 2 h post-injection and expressed as the % of injected dose per gram of tissue (mean ± standard deviation; statistical analysis by two-tailed *t*-test, N = 3-5; ****, *P* 0.0009).

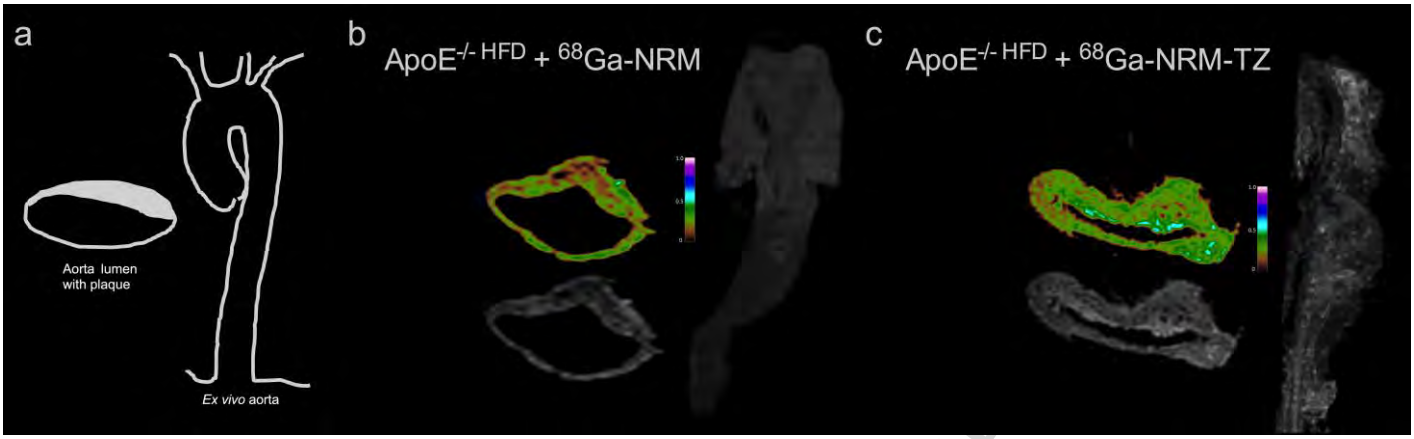

Figure 6. a) schematic representation of the ex vivo MR images; Axial magnetic resonance (pseudo-colored and normal contrast) and 3D MRP images from $ApoE^{-/-HFD}$ mice 24 h post-injection of Ab-TCO and 1 h post-injection of b), ^{68}Ga-NRM and c), ^{68}Ga-NRM-TZ.

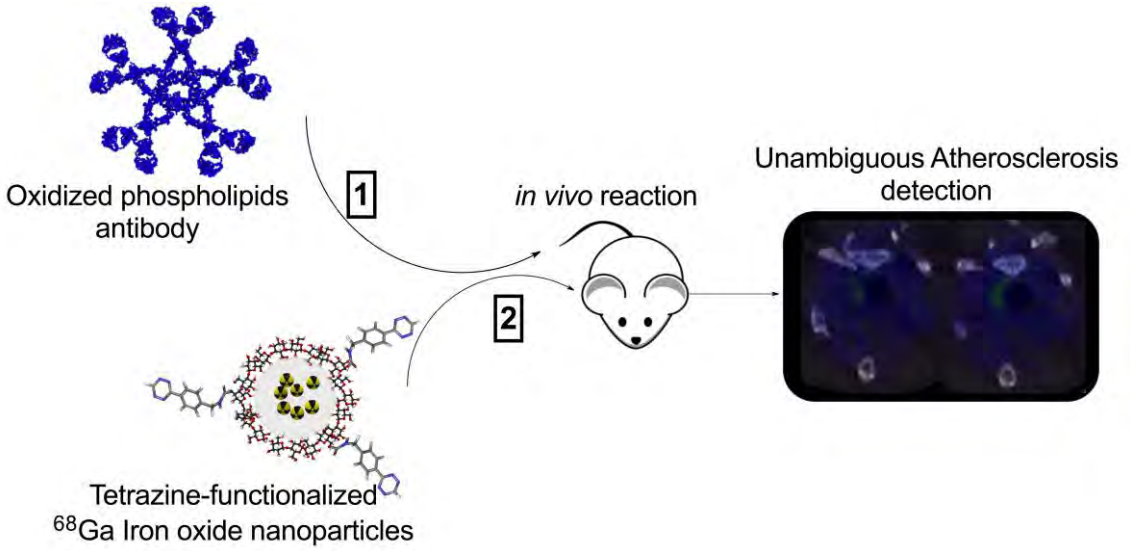

Unambiguous detection of atherosclerosis by the *in vivo* reaction of ^{68}Ga iron oxide nanoparticles with anti-oxidized phospholipids antibody